Reversed Nanoscale Kirkendall Effect in Au−InAs Hybrid Nanoparticles

Jing Liu,[†,¶] Yorai Amit,[‡,§,¶] Yuanyuan Li,[†] Anna M. Plonka,[†] Sanjit Ghose,[∥] Lihua Zhang,[⊥] Eric A. Stach,[⊥] Uri Banin,*[‡,§] and Anatoly I. Frenkel*[†,#]

[†]Department of Physics, Yeshiva University, New York, New York 10016, United States

[‡]The Institute of Chemistry and [§]The Center for Nanoscience and Nanotechnology, Hebrew University, Jerusalem 91904, Israel

[∥]National Synchrotron Light Source II, [⊥]Center for Functional Nanomaterials, Brookhaven National Laboratory, Upton, New York 11973, United States

[#]Department of Materials Science and Chemical Engineering, Stony Brook University, Stony Brook, New York 11794, United States

S *Supporting Information*

ABSTRACT: Metal−semiconductor hybrid nanoparticles (NPs) offer interesting synergistic properties, leading to unique behaviors that have already been exploited in photocatalysis, electrical, and optoelectronic applications. A fundamental aspect in the synthesis of metal−semiconductor hybrid NPs is the possible diffusion of the metal species through the semiconductor lattice. The importance of understanding and controlling the co-diffusion of different constituents is demonstrated in the synthesis of various hollow-structured NPs via the Kirkendall effect. Here, we used a postsynthesis room-temperature reaction between $AuCl_3$ and InAs nanocrystals (NCs) to form metal−semiconductor core−shell hybrid NPs through the "reversed Kirkendall effect". In the presented system, the diffusion rate of the inward diffusing species (Au) is faster than that of the outward diffusing species (InAs), which results in the formation of a crystalline metallic Au core surrounded by an amorphous, oxidized InAs shell containing nanoscale voids. We used time-resolved X-ray absorption fine-structure (XAFS) spectroscopy to monitor the diffusion process and found that both the size of the Au core and the extent of the disorder of the InAs shell depend strongly on the Au-to-NC ratio. We have determined, based on multielement fit analysis, that Au diffuses into the NC via the kick-out mechanism, substituting for In host atoms; this compromises the structural stability of the lattice and triggers the formation of In−O bonds. These bonds were used as markers to follow the diffusion process and indicate the extent of degradation of the NC lattice. Time-resolved X-ray diffraction (XRD) was used to measure the changes in the crystal structures of InAs and the nanoscale Au phases. By combining the results of XAFS, XRD, and electron microscopy, we correlated the changes in the local structure around Au, As, and In atoms and the changes in the overall InAs crystal structure. This correlative analysis revealed a co-dependence of different structural consequences when introducing Au into the InAs NCs. Therefore, this study of diffusion effects in nanocrystals has relevance to powerful concepts in solid-state nanochemistry related to processes of cation exchange, doping reactions, and diffusion mechanisms.
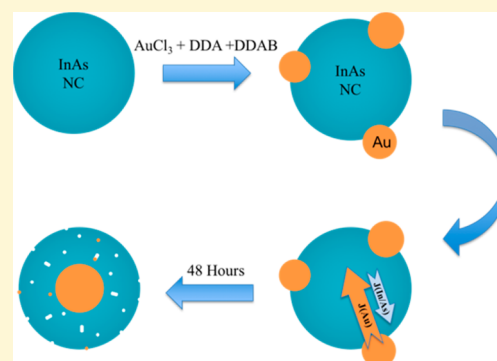
1. INTRODUCTION

Colloidal semiconductor nanocrystals (NCs), also known as quantum dots (QDs), have attracted significant attention due to their unique size-dependent optoelectronic properties.[1,2] Synthetic routes already offer high control over the size, composition, and shape of colloidal nanocrystals, leading to the demonstration of various geometries[3−7] and heterostructures[8−10] through wet-chemistry methods. Nowadays, there is a growing interest in the synthesis of hybrid nanoparticles (NPs), which combine disparate materials into a single system and often yield interesting synergistic properties.[11−15] Hybrid metal−semiconductor NCs were first presented by the growth of metal islands onto ZnO nanostructures[16] or TiO_2.[17−19] However, these reports had limited control over the size and location of the metal component. High control over the growth

of the metal domain was first presented by achieving anisotropic-selective growth of gold tips on CdSe[20,21] and CdS[22] nanorods to obtain a well-defined system with specific regions for the metal and semiconductor phases, a technique that was later expanded to other systems[23−27] and different synthetic routes, such as synthesizing the semiconductor component in the presence of the preformed metal structure[28,29] and through cation exchange reactions.[30] The emerging synergistic properties of such metal−semiconductor NPs were studied, showing enhanced light absorption,[28] altered photoluminescence,[31] exciton−plasmon interactions,[32,33] and

superior photoinduced charge separation,[34,35] which has led to their use in photocatalysis,[34,36−38] electrical,[28,39] and optoelectronic applications.[40,41] Therefore, rational design of hybrid nanostructures is an important task, requiring fundamental understanding of the underlying nanoscale reaction and diffusion mechanisms.

A fundamental effect that may accompany the formation of a hybrid metal−semiconductor interface is the possibility of diffusion of metals into the semiconductor lattice. One extensively studied process of diffusion of two materials across the nanoparticle surface is known as the nanoscale Kirkendall effect.[42,43] There, atomic species A with a lower diffusion rate enters the nanocrystal slower than the B species that diffuses outward from the nanocrystal. As a result, voids are formed in B, providing an interesting avenue for making hollow nanocrystals. Many examples of such mechanism were reported for the synthesis of hollow NPs including CoS and CoO,[42] ZnS,[44] PbS,[45] AuPt,[46] AlN,[47] and other metal oxides.[48−50] The opposite case, in which the outward species diffuses faster than the inner material, has been much less studied and was reported only for Pb and O, where the inward flow of oxygen ions is faster than the outward flow of Pb species, resulting in a solid PbO structure rather than a hollow one.[48] This "reversed nanoscale Kirkendall effect", if generalized to two solid materials, presents an intriguing new phenomenon and, possibly, a new way to synthesize unique nanoscale core−shell structures.

For both of the above effects, an essential question pertains to the mechanism by which the diffusion of metals through the semiconductor nanocrystal lattice occurs. In general, diffusion of impurities can occur on the surface, through a hopping mechanism[51−54] or by an atomic exchange process,[54−57] or they can diffuse into the lattice via substitutional or interstitial mechanisms.[58−61] However, diffusion in bulk semiconductors usually involves both interstitial and substitutional processes, and the two most prominent mechanisms are the Frank−Turnbull[58,59,62,63] and kick-out mechanisms.[58,59,62,64] The former occurs when an impurity diffuses interstitially through the lattice until an exchange event occurs and the impurity substitutes for a vacancy. In the latter, the impurity, which resides on an interstitial site, exchanges a lattice host atom by a kick-out action that results in the host atom occupying an interstitial site. This is an extensively studied topic in bulk semiconductors due to its significance in doped materials.[58,65] However, there have been few studies that reported the diffusion of impurities in nanostructured materials. Mokari et al. reported on the solid-state diffusion of gold in InAs NCs at room-temperature, which resulted in a Au−InAs core−shell NPs.[66]

In that work, presynthesized InAs NCs were reacted with gold(III) chloride in the presence of a reducing agent (dodecylamine) to yield islands of metallic gold on the surface of the NCs. Interestingly, imaging the Au−InAs hybrids after a period of 24 h, during which the sample was kept as a dry solid on the transmission electron microscopy (TEM) grid, revealed that the metal islands diffused from the surface of the NC to form a metal core surrounded by an amorphous InAs shell. X-ray diffraction (XRD) analysis indicated that the Au phase is compatible with bulk Au, the InAs crystal structure disappeared, and a weak signal of In_2O_3 was detected. A similar observation was made by Franchini et al. for PbTe NCs,[67] where reacting presynthesized PbTe NCs with $AuCl_3$ in solution, at moderate temperatures (60−90 °C), also resulted in a core−shell

structure where the gold is located in the center of an amorphous PbTe nanoparticle. The formation of such structures was explained by the fast diffusion of Au(0) species inward, balanced by Pb^{2+} and $Te^{2−}$ diffusion outward. Spatially resolved energy-dispersive X-ray (EDX) analysis determined that the core consists of Au only, whereas the shell is a mixture of Pb, Te, and Au. However, both studies lack the ability to identify the mechanism through which Au diffuses in the semiconductor lattice.

Recently, we employed advanced X-ray absorption spectroscopy techniques to study the local structure of Ag and Cu doped InAs NCs, employing a similar synthetic route as presented above.[68−70] Interestingly, we found that reacting InAs NCs with a wide range of Cu concentrations, at room temperature, results in a purely interstitial doping scheme, up to a very high level of Cu incorporation, without evidence of the formation of a metal structure.[68] For Ag doped InAs, however, we identified two regions that depended on the ratio between the number of Ag species in the reaction vessel and the number of InAs NCs. Ag was found to initially behave as a substitutional dopant, and, only above a threshold concentration, metal structures were formed on the InAs NC surface, yielding hybrid Ag−InAs nanoparticles.[69] In neither case did we observe the phenomena of metal agglomeration within the NC lattice, nor did we observe any changes in the local structure surrounding the impurity atoms, even after extended periods of time.

In this work, we present a study of the structural evolution of InAs NCs during the addition and solid-state diffusion of Au atoms. We employed time-resolved (TR) X-ray absorption fine-structure (XAFS) spectroscopy in conjunction with scanning transmission electron microscopy/electron energy loss spectroscopy (STEM/EELS) and TR XRD to investigate the real-time Au diffusion process in 5 nm InAs NCs. Analysis of this system by XAFS is much more challenging compared to that of other doped systems because of the proximity of the As K-edge (11 867 eV) and Au L_3-edge (11 919 eV). In the case of extended X-ray absorption fine structure (EXAFS) signals that originate from the two nearby absorption edges, both the lower and higher energy element EXAFS signals overlap at the higher energy edge region. This presents a particular challenge to the analysis of this system where As, the lower energy edge element, is part of the host structure and Au, the higher energy element, is the impurity. Hence, for structural analysis of both the impurity and the host, it is necessary to separate their contributions in EXAFS. Here, this was achieved through the use of EXAFS data analysis methods developed by us earlier for this particular purpose.[71] We studied the effect of the Au concentration, in terms of the Au-to-NC ratio in the reaction solution, on the diffusion rate and the resulting structure of the Au phase, as well as the structural degradation of the InAs lattice. We found that there is a strong driving force for Au diffusion through the NC lattice, resulting in a core metallic structure inside the NC. This occurs even at low Au/NC ratios, where no evidence of metallic structures on the NC surface are observed. We monitored the structural evolution from the viewpoint of both host (In, As) atoms by analyzing their K-edge XAFS data and impurity (Au) atoms by analyzing their L_2- and L_3-edge XAFS data. From the host side, the rate of the structural degradation strongly depends on the Au/NC ratio, whereas the Au signal shows much slower changes. The degradation of the NC lattice is accompanied by the formation

of In−O bonds, which acts as a marker for investigating the process of Au incorporation and diffusion through the lattice.

As a whole, a multimodal investigation of this complex system reveals features of a reversed nanoscale Kirkendall effect in which the flux of Au through the InAs NC lattice is faster than the reverse flux of In. The process is enabled by a kick-out type mechanism, in which Au substitutes for In and As in the InAs structure. The final hybrid structure contains a nanocrystalline face-centered cubic Au core, surrounded by an InAs shell that is disordered and porous. Increasing the Au/InAs NC ratio leads to both large Au cores and more substantial disorder in the InAs shell that surrounds that core. This eventually becomes a large amorphous shell at high Au/InAs NC ratios. The reversed nanoscale Kirkendall effect observed and studied in this Au−InAs system may also provide an additional route to the synthesis of nanocrystal core and amorphous/disordered shell structures of other pairs of materials, thus enriching the library of colloidal nanoscale building blocks.

2. EXPERIMENTAL SECTION

2.1. Synthesis. Colloidal InAs NCs were synthesized following a well-established wet-chemical synthesis.[72] Precursor solutions containing (TMS)$_3$As (tris(trimethylsilyl)arsine) and InCl$_3$ (indium(III) chloride) were prepared in a nitrogen glovebox and kept under inert conditions throughout the reaction. A solution of distilled trioctylphosphine (TOP) was evacuated for 30 min and heated at 300 °C. The nucleation solution (2:1 In/As) was rapidly injected, and the solution temperature was decreased to 260 °C. The growth solution (1.2:1 In/As) was gradually introduced to the solution, allowing particle growth until the desired size was reached. Narrow size distributions were further achieved through size-selective precipitation performed in a glovebox by adding methanol to the NC dispersion and filtering the solution through a 0.2 μm polyamide membrane filter.

Hybrid InAs−Au nanoparticles were obtained via a room-temperature solution-phase reaction reported previously.[66,70] Briefly, a gold(III) chloride solution was prepared by dissolving 10 mg (0.033 mmol) of the metal salt (AuCl$_3$), 75 mg (0.16 mmol) of didodecyldimethylammonium bromide (DDAB), and 180 mg (0.95 mmol) of dodecylamine (DDA) in 10 mL of anhydrous toluene. Calculated amounts (v/v) of the impurity solution were added to a suspension of InAs NCs, according to the desired Au/NC ratio, while stirring. Au ranged from 8×10^{-6} to 8×10^{-5} mol for a solution of 1.6 $\times 10^{-8}$ mol of 5 nm (in diameter) InAs NCs. These values are below as the Au/NC ratio in solution, ranging from 500 to 5000, respectively.

The reaction was performed under inert conditions in a glovebox and terminated after 5 min by adding methanol and isolating the Au−InAs NCs through precipitation.

2.2. Electron Microscopy. Scanning transmission electron microscope (STEM) images were captured using a Hitachi HD2700C operated at 200 kV at the Center for Functional Nanomaterials in Brookhaven National Laboratory. The spatial resolution for imaging was about 1.0 Å. The probe current was in the 50−100 pA range. The STEM images were taken using a high-angle annular dark-field (HAADF) detector. The frequency distribution of Au core diameters in the sample with a Au-to-NC ratio of 1000 was measured over 135 InAs NCs. Elemental line scans with a step size of 1.4 Å were made with a high-resolution electron energy loss spectroscopy (EELS) detector (Gatan Enfina-ER). We extracted the Au and As EELS signals from the EELS spectrum using a power-law background model and an integration window in advance of the Au N- and As M-edges.

2.3. X-ray Absorption Spectroscopy Experiment. TR In K-edge, As K-edge, Au L$_3$-edge, and Au L$_2$-edge XAFS measurements were taken from Au−InAs samples with 1000 and 2000 Au/NC ratios. These samples were dissolved in toluene, sealed in a custom-made liquid cell, and measured at beamline 5BM-D of the Advanced Photon

Source (APS). The In and As K-edge data of InAs control samples were collected at APS beamline 5BM-D as well. The TR In K-edge data of solid Au−InAs samples with 500, 1000, 2000, 3000, and 5000 Au/NC ratios were collected at SSRL beamline BL2-2. These samples were spread on Kapton tape and mounted in a sample chamber. The samples were prepared under inert conditions in a glovebox. All samples were sealed in the glovebox prior to their transfer to the beamline, where they were kept under inert conditions during the measurement. The experiments were performed in transmission mode. From 3 to 6 scans were taken for each edge to improve the signal-to-noise ratio.

2.4. XAFS Data Analysis. XAFS data processing and analysis were done using Athena and Artemis software within the IFEFFIT package.[73,74] For the In K-edge data, we used a linear combination analysis method (*vide infra*) for XANES data and theoretical fitting for EXAFS data. To fit the In K-edge EXAFS data, we accounted for two contributions, In−As and In−O, which represent a bond between In and a low-Z element, as discussed in greater detail below.

A recent strategy for deconvoluting the overlapping absorption edges[71] was applied to the As K- and Au L$_3$-edge data. Specifically, the As−In contribution to the Au L$_3$-edge EXAFS from the lower energy As K-edge was taken into account. The scaling factor used to normalize the Au L$_3$-edge EXAFS was defined as $\frac{\Delta\mu_{0,As}}{\Delta\mu_{0,Au}}$, where $\Delta\mu_{0,As}$ and $\Delta\mu_{0,Au}$ represent the jumps in the absorption coefficients at corresponding absorption thresholds (E_0). The edge step ($\Delta\mu$) is defined as the vertical difference between the pre-edge and post-edge lines at the edge energy E_o (Supporting Information Figure S1). The correction to the photoelectron energy origin for the As K-edge EXAFS, which is 52 eV lower in energy than the nominal value of the Au L$_3$-edge, is no longer a single adjustable parameter, as in conventional EXAFS analysis. It is now defined with respect to the Au L$_3$-edge energy as $\Delta E_{o,As} - (52 + \Delta E_{o,Au})$. For the Au L$_3$-edge analysis, As−In paths contributes to the Au L$_3$-edge EXAFS data; thus, we performed fits for the In K-edge and Au L$_3$-edge simultaneously for the Au−InAs (1000 Au/NC) sample by constraining the parameters of In−As pairs (bond lengths and their disorders) to be the same, as measured from each edge. The paths included in the fitting were the Au−As, Au−Au, and As−In pairs for the Au L$_3$-edge and the In−O and In−As pairs for the In K-edge.

For the Au L$_2$-edge analysis, theoretical FEFF6 fits were performed simultaneously for all time-dependent EXAFS data with the same Au concentration. The value of the amplitude reduction factor, S_0^2, was obtained from the fitting of Au foil to 0.993 ± 0.051 and fixed to 0.993 in the fits. The photoelectron paths connecting the Au−As and Au−Au nearest-neighboring pairs were included to the theoretical EXAFS signal with the same energy shift (ΔE_0) and individually varied coordination number (N) and bonding distance correction (ΔR) and its means square disorder, or Debye−Waller factor (σ^2).

The results obtained for the Au L$_3$-edge and Au L$_2$-edge were found to be in qualitative agreement with each other, as explained in greater detail below. This agreement validates our data analysis procedure used for the Au L$_3$-edge analysis that overlaps with the As K-edge.

2.5. X-ray Diffraction. XRD data were collected at the XPD beamline of the National Synchrotron Light Source II, Brookhaven National Laboratory, using a monochromatic beam with an incident energy of 42 keV (corresponding to a wavelength of 0.2952 Å). Diffraction data were collected in transmission mode with an amorphous silicon-based flat panel 2D detector (PerkinElmer) mounted orthogonal to and centered on the beam path and were reduced to 1D profiles using the Fit2D software. The sample-to-detector distances and tilts of the detector relative to the beam were refined using a LaB6 powder standard. Noticeable artifacts in the images such as the beam stop or dead pixels were masked. Due to the small particle size and low concentration of particles in the samples, the diffraction peaks are very broad and are too weak to perform any quantitative analysis using existing structure refinement methods. However, a qualitative comparison of the diffraction peaks from InAs and Au provides clear indication of interdiffusion of the two-phase components, as discussed in greater detail below. The ratio between
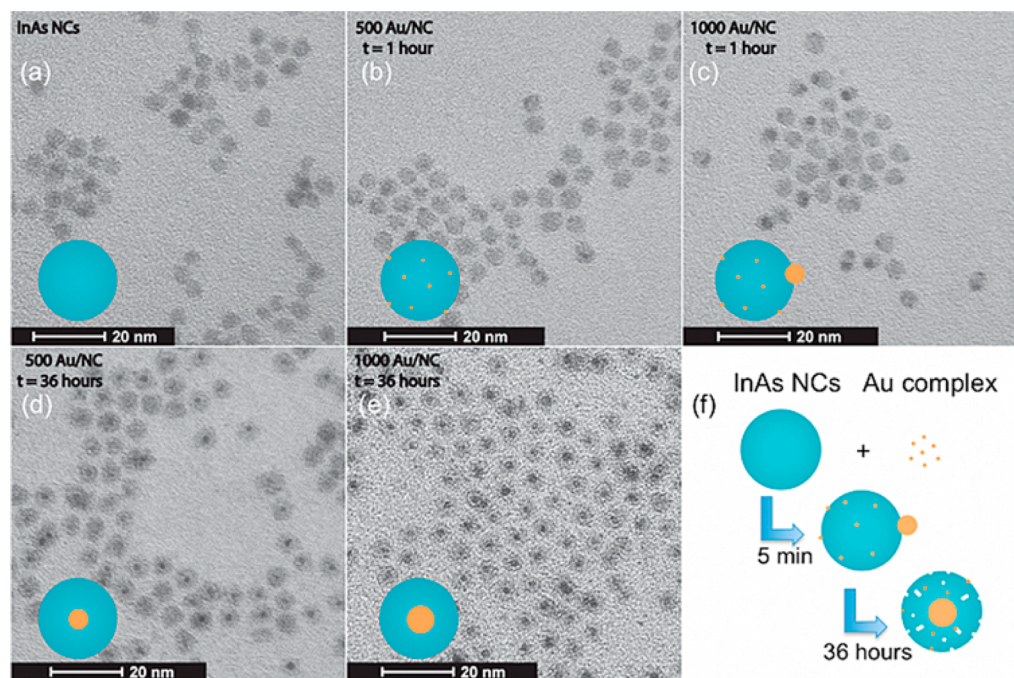
Figure 1. TEM images of (a) as-synthesized 5 nm InAs NCs, (b) InAs NPs 1 h after reaction with 500 Au atoms per NC (in solution), (c) InAs NPs 1 h after reaction with 1000 Au atoms per NC, (d) InAs NPs 36 h after reaction with 500 Au atoms per NC, and (e) InAs NPs 36 h after reaction with 1000 Au atoms per NC. Schematics of the diffusion process of Au into the core of the InAs NCs are shown in the bottom left of each panel.

the InAs (220) and Au (111) reflection intensities was estimated based on the maximum height of the peaks. Before estimating the height, each pattern was background-corrected and normalized with baseline-scattered intensity.

3. RESULTS AND DISCUSSION

3.1. Synthesis of Au–InAs Hybrid Nanoparticles.
Colloidal InAs NCs were synthesized using a well-established synthesis process,[72] followed by size-selective precipitation to obtain narrow size distributions. The presynthesized InAs NCs were reacted with Au by mixing a suspension of InAs NCs in toluene with a gold(III) chloride solution containing the metal salt ($AuCl_3$), DDAB to stabilize the metal salt in the organic solution, and DDA, which acts as a reducing agent. Different Au concentrations were used in the reaction.

As seen in Figure 1, approximately 1 h after the reaction of the 500 Au/NC ratio, no metallic features were observed on the NC surface. Increasing the ratio to 1000 Au/NC reveals higher contrast regions on the NC surface, indicating the formation of small Au clusters. After 36 h, both samples reveal the formation of a higher contrast core material (Au) surrounded by a lower contrast shell material (InAs). The size of the Au core is larger for higher Au-to-NC ratios, as seen both in the TEM images (Figure 1) and HAADF STEM images (Figure 2). Formation of the Au core is confirmed by quantitative STEM/EELS analysis (Figure 2d−f). STEM images of the pure InAs NCs reveal clear lattice fringes (Figure 2a), whereas in the hybrid Au−InAs NPs, lattice fringes were observed in the Au core (Figure 2c, inset), but no fringes were observed in the InAs shell. This is a clear indication of disordering of the InAs structure due to Au incorporation in InAs.

3.2. XAFS Data and Analysis.
To monitor structural changes in both the host (InAs) and the Au phases, XAFS data were measured at different aging times and at different Au/NC ratios. TR XAFS was measured at the In K-edge to monitor the
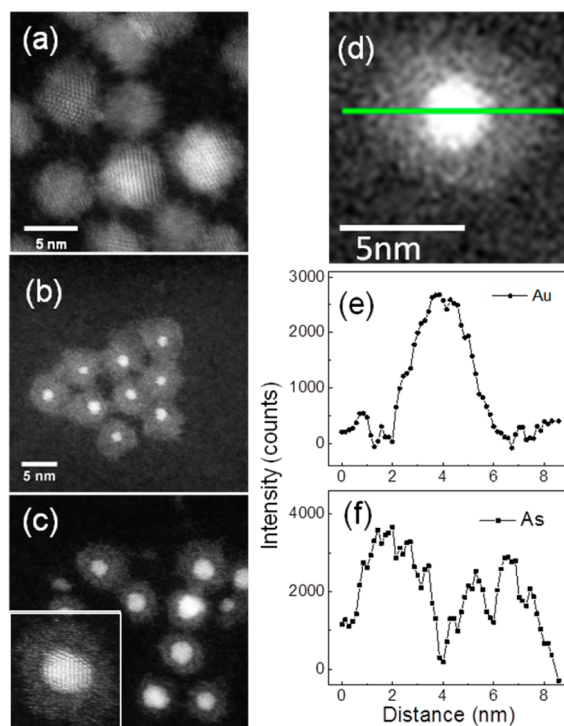

Figure 2. High-angle annular dark-field STEM images of as-synthesized 5 nm InAs NCs (a) and Au−InAs NPs (∼1 week after reaction of 1000 (b) and 4000 (c) Au atoms per NC). Atomically resolved fringes in the Au core are seen in the inset (6.6 × 7.2 nm) of panel c. Images (b) and (c) share the same scale bar. The EELS line-scan profiles (d) at Au N- and As M-edges (e, f) of single Au−InAs NPs taken about 1 week after reaction of 1000 Au atoms per NC.

changes in the average electronic and local structure of In atoms in the Au−InAs system during the solid-state diffusion
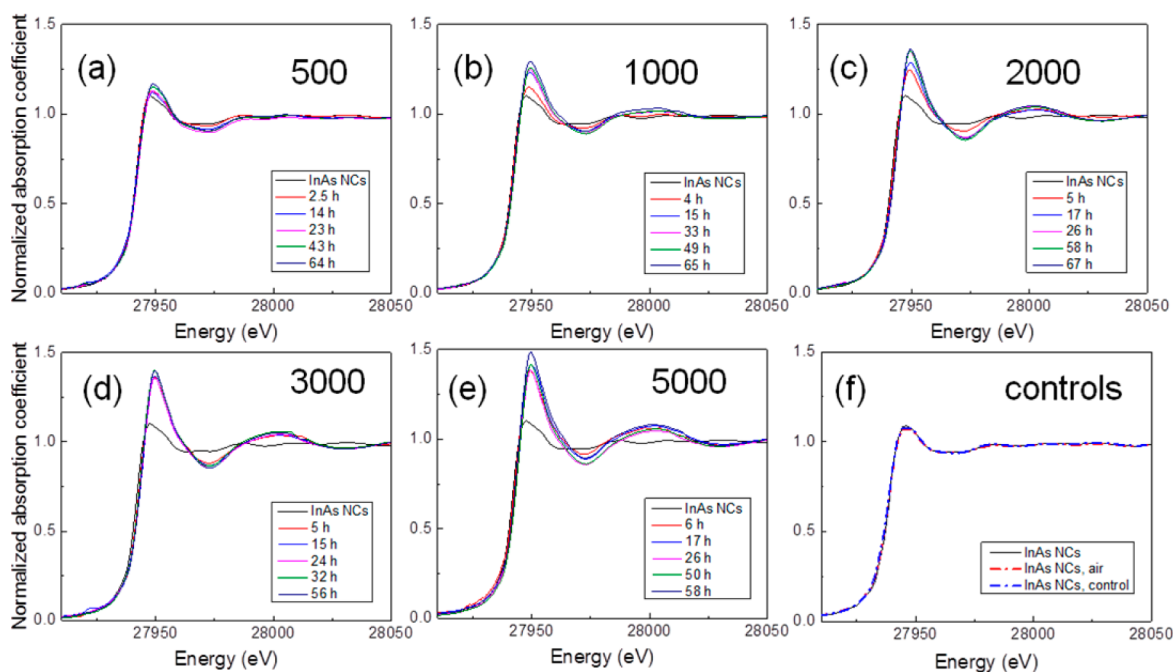
Figure 3. Time-resolved XANES data at the In K-edge of Au−InAs NPs, with nominal Au/NC ratios shown in the top right (a−e) and InAs control samples (f). The Au−InAs NPs were reacted with 500, 1000, 2000, 3000, and 5000 Au atoms per NC, as indicated. The aging time is defined as the time elapsed after the synthesis.
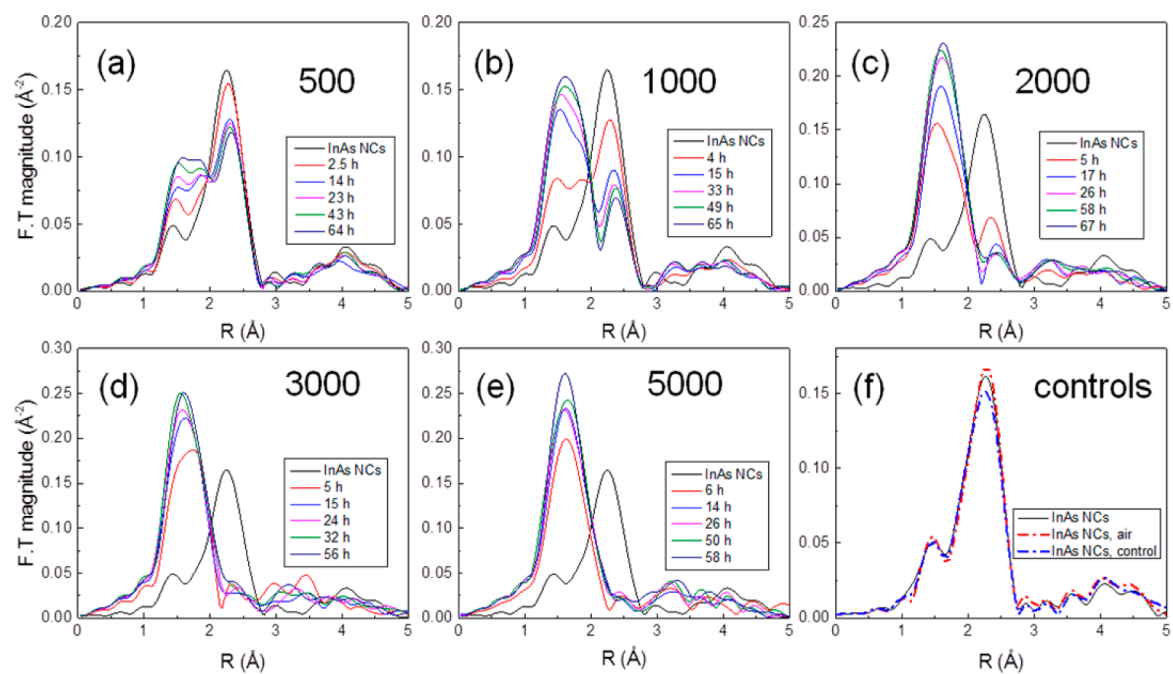

Figure 4. Fourier transform magnitudes of k-weighted In K-edge EXAFS data (a−e) of Au−InAs NPs with representative Au/NC ratios and InAs control samples (f). The Au−InAs NPs were reacted with 500, 1000, 2000, 3000, and 5000 Au atoms per NC, as indicated. The aging time is defined as the time elapsed after the synthesis.

process. The In K-edge TR XANES data measured for different Au/NC ratios are plotted in Figure 3a−e. The intensity of the In K-edge main peak, corresponding to the 1s−5p electronic transition, increases with the introduction of Au into the system (for any given time) and also changes over time (for any given dopant concentration), indicating a change in the electronic properties of In atoms.

We note the existence of isosbestic points in the X-ray absorption near-edge structure (XANES) spectra for all Au/NC

ratios, which is an indication of the presence of only two distinctly different states of In, mixed in different fractions, that can change with time and with the Au/NC ratio. The first state corresponds to the starting InAs NC structure and the second, as we explain in greater detail below, to the disordered In−O structure.

As a control, we measured the as-synthesized InAs NC samples exposed to ambient atmospheric conditions (for a period of 3 days) or upon exposing the NCs to the ligand
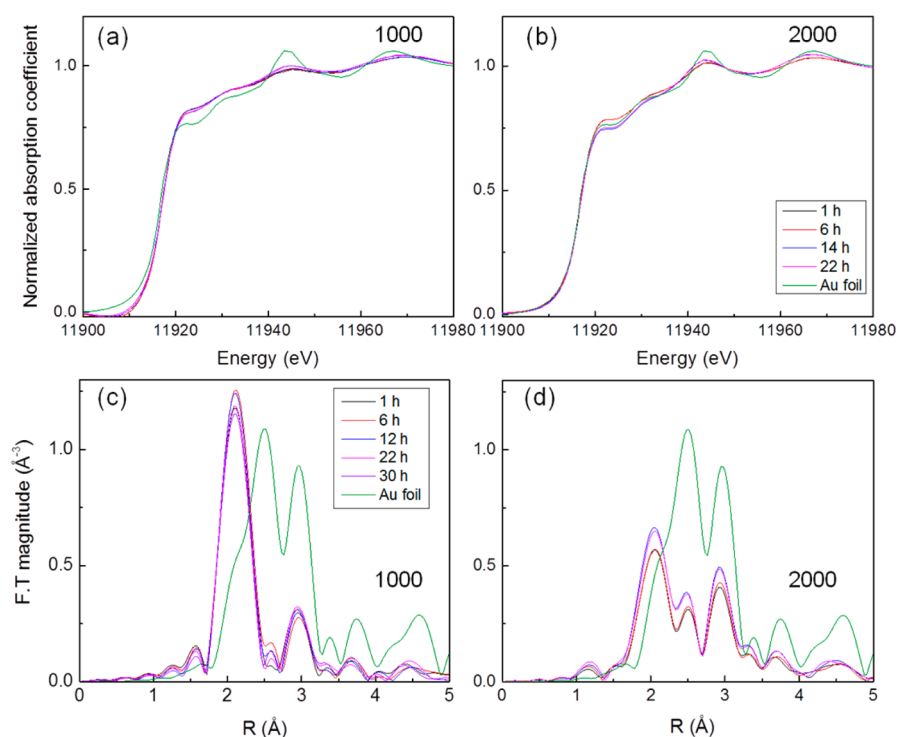
Figure 5. Time-resolved XANES data at the Au L$_3$-edge (a, b) and FT magnitudes of k^2-weighted EXAFS data (c, d) of Au−InAs NPs with 1000 and 2000 Au/NC in the reaction, respectively.
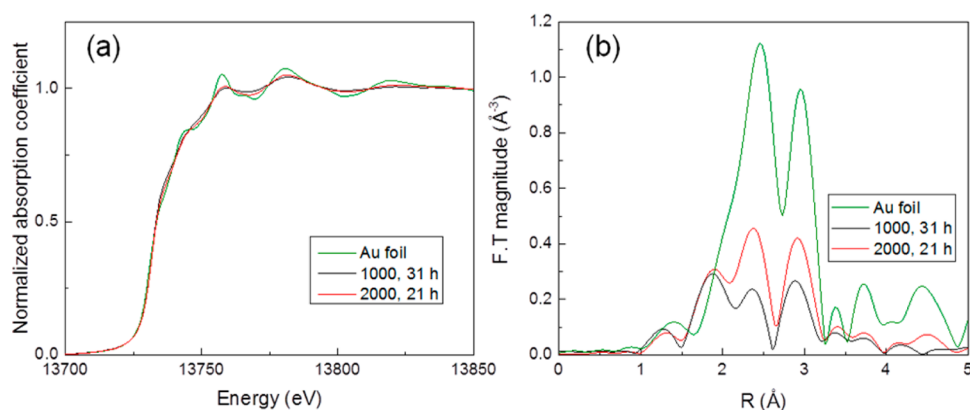

Figure 6. XANES data at the Au L$_2$-edge (a) and Fourier transform magnitudes of k^2-weighted EXAFS data (b) of Au−InAs NPs (reacted with 1000 and 2000 Au atoms per NC, respectively) at selected aging times, together with the data for Au foil.

solution without the metal salt (Figure 3f). These control changes exhibited almost no changes compared to the Au-doped InAs NCs of the same sizes showing a series of structural and electronic evolutions with time and Au concentrations.

The Fourier transform magnitudes of the k-weighted In K-edge TR EXAFS signals are shown in Figure 4a−e. The representative In K-edge k^2-weighted $\chi(k)$ data are shown in Figure S3a,b. The main peak for pure InAs NCs at around 2.2 Å is due to the As atoms that surround each In atom in the lattice. For Au−InAs NPs samples, the intensity of this peak decreases with time, whereas a low-R peak appears and grows in intensity over time, in qualitative agreement with the trend shown in Figure 3a−e for the In K-edge XANES data. In the quantitative data analysis, various binding species were considered as a possible origin of this new emerging peak, including In−Au, In−N, and In−O. In−Au bonding was found to be improbable due to the short bond length, and the fitting failed when this

bonding was included. While we cannot distinguish between In−N (originating, possibly, from the ligand) and In−O, it is unlikely that the contributions from In−N bonds would change as much over time in the solid state, whereas an evolution of an In−O peak is more reasonable if we consider the presence of an oxygen moiety near the sample. However, it is noteworthy that the resulting oxide phase does not appear in the control samples (Figure 4f), in agreement with the stability of their XANES spectra (Figure 3f). Hence, the evolution of the observed In low-Z peak is directly connected to the reaction of the Au atoms with the InAs NCs. In what follows, we will use the formation of the In−O peak as a marker of the decomposition of the InAs lattice in response to the diffusion of Au atoms. As a summary of the In K-edge XANES and EXAFS data, we conclude, qualitatively, that the amount of disorder in the InAs NC structure correlates with the Au/NC ratio, namely, the greater the latter, the larger is the former.

The TR XAFS data for Au−InAs NPs with 1000 and 2000 Au/NC ratios, measured at the As K- and Au L_3-edge, are shown in Figure 5 and at the Au L_2-edge in Figure 6 (more TR XAFS data at the Au L_2-edge are shown in Figure S4). The representative Au $L_{2,3}$-edge k^2-weighted $\chi(k)$ data are shown in Figure S3c,d. In the Au L_3-edge XANES data (Figure 1a,b), the metallic Au feature is observed for all spectra with reduced oscillations compared to the bulk, as expected for nanosized gold.[75] The As K-edge EXAFS is included in the extracted Au L_3-edge EXAFS due to the proximity of their absorption energies, as discussed in the Experimental Section (Figure S2). As seen in Figure 5c,d, the very strong contributions from As−In bonding can be identified at ∼2 Å along with the Au−As and/or Au−Au contributions at longer distances. Therefore, the contribution from As K-edge EXAFS, namely, As−In first nearest-neighbor contribution, was considered in the fitting of the Au L_3-edge EXAFS, in addition to the Au−As and Au−Au contributions. This is in contrast to the Au L_2-edge data (Figure 6) that contain only Au−Au and Au−As contributions. Although the two sets of data measured from the Au L_3 and L_2 edges contain similar information, both of them are important for successful analysis of low and high Au/NC ratios. Indeed, for low Au compositions, the As−In contribution dominates the Au L_3-edge spectra (Figure 5c). That is an excellent edge, therefore, to measure As−In pairs, but it is not good for the Au−As and Au−Au contributions that are weak and difficult to analyze. For the same compositions, Au L_2-edge data can be used to recover the two latter contributions. For large Au/NC ratios, both Au L_3- and Au L_2-edge data can be used interchangeably. We used both of them to compare their results for the EXAFS analysis of the Au−As and Au−Au contributions, as obtained for either edge at high Au/NC ratios. It is important to perform this comparison in order to validate our procedure of the deconvolution of the EXAFS spectra of the As K-edge and Au L_3-edge. If the procedure is correct, then both sets of results (for the Au L_2- and L_3-edge) should be similar, within uncertainties.

The positions of the absorption edge and main features in the Au L_2-edge XANES regime of Au−InAs NPs (Figure 6a) are very similar to those of bulk Au but with smaller oscillation amplitudes, which are typical for nanoscale gold particles, i.e., the same observation as the one just made for the Au L_3-edge (Figure 5a). The overall similarity with the bulk indicates that the Au atoms are already in an environment similar to that of the metal state in the system at early stages after the reaction (Figure S4) due to rapid nucleation of Au on the NC surface. The same conclusion can be made from Figure 5. R-space spectra of Au L_2-edge EXAFS (Figure 6b) show two different contributions. The double peak above 2 Å corresponds to the Au−Au contribution, whereas the lower-R peak (below 2 Å) corresponds to Au−As contribution. From the time-dependent data, shown in Figures 5 and S4, we learn that Au nucleates relatively fast for both 1000 and 2000 Au/NC ratios because the metallic features set in already ca. 1 h after the reaction.

Despite the fact that EXAFS analysis of the nearest-neighbors environment of As atoms can be analyzed only from the Au L_3-edge, the As K-edge XANES region is sufficiently well separated from the Au L_3-edge for its separate examination. Figures S5 demonstrates that the intensity of the main peak of the As K-edge XANES region increases with time due to the diffusion of Au into the NC lattice for both 1000 and 2000 Au per NC ratios, demonstrating that the electronic properties of As atoms change similarly to those of In atoms. Specifically, both As and

In edge shape changes are consistent with the transfer of electron density away from both atoms, as possible, e.g., when As−O and In−O bonds are formed. Such a common trend is expected because, as demonstrated from the In edge data, Au diffusion leads to the breaking of In−As bonds. Hence, both In and As edge data will be affected. In validation of the role of Au in the In−As bond breaking, Figure S6 shows no visible changes in As K-edge XANES and EXAFS behaviors in the pure InAs NC sample exposed to air for 3 days or upon exposing the NCs to the ligand solution without the metal salt. Figures 3f and 4f conveyed the same information, as seen from the In K-edge.

Results of analysis of the TR EXAFS data of Au−InAs NPs collected at the Au L_2-edge provide quantitative information on the behavior of the Au species. It is confirmed, from the analysis of EXAFS at the Au L_2-edge of 1000 and 2000 Au/NC samples, that the Au region forms very rapidly, within ca. 1 h from the reaction (Figure S7). Only the Au−Au and Au−As contributions were used in fitting the data (Figures S7 and S8 and Tables S1 and S2). The Fourier transform parameters used in fitting are shown in Table S4. As shown in Table S1 and S2, the coordination number (CN) of Au−Au pairs obtained from the fitting is about 6.5 ± 1.4 for the 1000 Au/NC ratio and 8.4 ± 0.8 for 2000 Au/NC ratio at 2 h after synthesis and remains relatively stable, with only a small increase to about 7.1 ± 0.8 for the 1000 Au/NC ratio and 8.8 ± 0.9 for the 2000 Au/NC ratio, after about 20 h. The Au−Au interatomic distance (Tables S1 and S2) was found to be 2.81 Å, which is shorter than the value of bulk gold (2.88 Å). This finding is consistent with the finite size effect that is known to cause shorter Au−Au bond lengths in nanosized structures compared to their bulk counterparts.[76−78]

EXAFS analysis demonstrated that Au exists in two forms in the InAs QD. In one form, it is mixed in the InAs lattice, forming Au−As pairs, and in the other, it forms Au metallic phase. Thus, the effective coordination number, ν_{AuAu}, which describes the Au−Au pairs with respect to the metal phase only, can be defined as

$$\nu_{AuAu} = N_{AuAu} / \left(1 - \frac{N_{AuAs}}{4}\right) \qquad (1)$$

where N_{AuAu} and N_{AuAs} are the apparent coordination numbers from the EXAFS fitting for Au−Au and Au−As, respectively. Assuming a model in which Au atoms substitutes for In atoms in the InAs phase, for each Au atom there should be four As atoms at the nearest-neighboring positions. Thus, $\frac{N_{AuAs}}{4}$ contains the fraction of all Au atoms in this substitutional location, and $\left(1 - \frac{N_{AuAs}}{4}\right)$ is the fraction of Au atoms in the Au core. As shown in Tables S1 and S2, the Au−Au coordination number is relatively stable at about 6.7 for the 1000 Au/NC ratio from 2 to 12 h after synthesis, and it increases above 8 after 22 h. For comparing the size of the Au core inferred by EXAFS analysis with that imaged by STEM, the effective coordination number is a better quantity than the apparent coordination number (N), in analogy with other heterogeneous systems of this nature.[79,80] Using eq 1, we calculated the effective average Au−Au coordination numbers for Au−InAs NPs (1000 and 2000 Au/NC) based on the Au L_2-edge fitting results for which the largest values were 8.5 and 9.5, respectively. For the purpose of estimating the Au core size from the effective coordination numbers, we adopt regular cuboctahedral cluster models. The
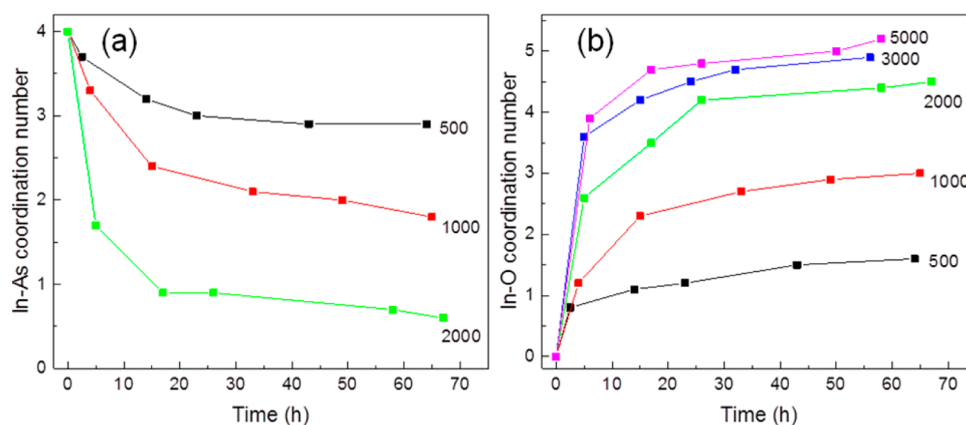
Figure 7. Comparison of coordination numbers of (a) In−As and (b) In−O pairs in Au−InAs NPs for various Au/NC ratios as a function of aging time (elapsed after the beginning of doping reaction), obtained from the best fit of the time-resolved In K-edge EXAFS data.

model clusters that correspond to those coordination numbers contain 147 (the CN is 8.98) and 309 (the CN is 9.63) Au atoms, respectively, and are ca. 1.7 and 2.2 nm in size.[81] The so obtained size of the Au core for the 1000 Au/NC sample is in good agreement with the 1.5 nm value measured by STEM imaging (Figures 2 and S2) and is consistent with the EELS line profile shown in Figure 2. In addition, it is also consistent with the reduction of the Au−Au distance compared to the bulk Au foil (*vide supra*).

While the agreement between different probes (EXAFS and STEM) is very good, STEM images not only provide proof that the Au atoms nucleate but also show directly that the stability of the NC scaffold is compromised upon the diffusion of Au at high Au/NC ratios. Whereas the InAs shell remains whole and the overall NP size does not seem to change for the 1000 Au/ NC sample (Figure 2b), the 4000 Au/NC sample exhibits regions where the InAs shell breaks off the Au core (Figure 2c). Au diffusion at high concentrations thus has a destructive effect on the NC lattice. A different view of the effects of Au diffusion on the structure of the InAs host is available through the coordination numbers of the In−As and In−O bonds obtained from EXAFS analysis (Figure 7 and Table S3; the Fourier transform parameters used in the fitting are shown in Table S5). The coordination numbers of In−As pairs decrease with time and Au concentration, whereas those of In−O pairs increase with time and Au/NC ratio, indicating the gradual breaking of In−As bonds and forming of In−O bonds during Au diffusion. Figure 7 also indicates that the nucleation of Au occurs relatively fast during and after synthesis and that the further growth of Au is relatively slow. Accordingly, the coordination number of Au−As is nearly unchanged during the measurements (Tables S1 and S2).

We note that the Au−As distances (Tables S1 and S2) are similar to the In−As ones; hence, the model of Au incorporation into the InAs lattice is substitutional, not the interstitial, which would have been characterized by extremely short Au−As distances as formation of In−Au nearest neighbors. The interstitial model, possessing such properties, was previously reported by us for Cu doped InAs NCs.[68] Hence, the kick-out, not the Frank−Turnbull, mechanism is likely at play.

To identify the origin of the O species in the InAs NCs, we performed a series of control experiments. We measured the XANES and EXAFS of (i) as-synthesized InAs NCs, (ii) InAs NCs that were exposed to atmospheric conditions for 72 h, and

(iii) InAs NCs that were reacted with the same precursor solution without the metal salt (i.e., containing similar concentrations of DDA and DDAB). Results shown in Figures 3, 4, and S4 show little or no changes among these three samples. We thus conclude that the diffusion of Au into InAs NCs triggers the formation of In−O bonds. Considering that only In−O bonds are identified, we conjecture that the mechanism of diffusion involves the kicking out of In atoms by Au. Correspondingly, as the Au continues to diffuse to the center of the NC through the kick-out mechanism, the InAs NC structure becomes amorphous.

3.3. XRD Data and Analysis. In addition to STEM data that provide statistical information about the effects of Au diffusion on different InAs NCs and XAFS data that characterize the local structure of Au, In, and As atoms, we analyzed XRD data that provide long-range information on both the Au and InAs phases and their relative changes with time and Au concentration. Thus, a combination of the three measurements will help to better understand the co-dependence of the different changes induced in InAs NCs upon Au diffusion.

TR XRD measurements of Au−InAs NPs were performed on the representative 1000 Au/NC sample. In Figure 8a, the diffraction peaks corresponding to InAs and Au are identified. Both sets of diffraction peaks broaden and shift to higher 2θ values compared to the corresponding bulk values, which is typical for nanoparticles due to their smaller lattice parameter and is consistent with the EXAFS fitting result of the reduced Au−Au distance (Figure S7 and Tables S1 and S2). Noticeably, the diffraction peaks of In_2O_3 are absent, which is in line with the lack of long-range order in In−O interactions, although In−O bonding was observed from EXAFS. Relative changes of Au and InAs crystalline volumes were studied for the 1000 Au/NC sample by using the relative changes in the InAs/Au peak intensities as a function of time. This ratio was found to monotonically decrease with time, implying that the long-range order of InAs is reduced relative to the increase in Au ordering. Hence, the combination of EXAFS and XRD results demonstrates that the structural changes of InAs NCs occur at both short- and long-range scales. In addition, the kinetics of growth of the Au phase (Figure 8a, inset), extracted from data in Figure S9, shows a two-step behavior, in qualitative agreement with the data obtained from XAFS.

3.4. Unifying Discussion. Following the above presentation of the data obtained by complementary STEM, XAFS, and
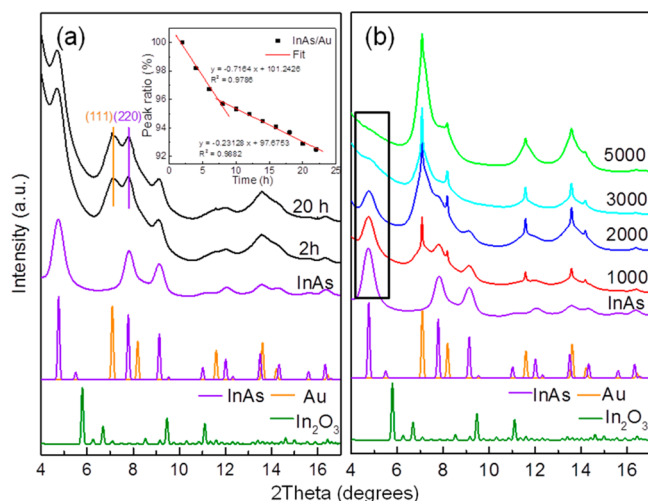
Figure 8. XRD patterns of (a) Au−InAs NPs with a 1000 Au/NC ratio collected at 2 and 20 h after synthesis (the inset shows the peak ratio between the InAs (220) and Au (111) peaks) and (b) Au−InAs NPs with different Au/NP ratios, taken 2 days after synthesis.

XRD experiments, we now attempt to unify these observations. XANES and EXAFS data provide information on the chemical, electronic, and/or structural changes in the In, As, and Au environments. We interpret the changes in the In environments in terms of the volume fractions of InAs NCs that remain unaffected by Au diffusion and the volume fractions of the In−O regions formed. The former quantity can be obtained by normalizing the In−As coordination numbers measured by EXAFS by 4, which is the stoichiometric value of In−As coordination number. The volume fractions of the In−O regions can be estimated either by normalization of the In−O coordination numbers by 6, its stoichiometric value in the oxide, or from the linear combination analysis (LCA) of the In K-edge XANES data (as shown in Figure S10). LCA was carried out for the TR XANES of representative Au/NC ratios shown in Figure 3. The XANES spectra of pure InAs NCs and Au−InAs with a 5000 Au/NC ratio collected at 58 h (corresponding to the disordered final state) were used as two basis sets for the fitting.

Figure 9 shows the volume fractions of In−As and In−O regions for different Au/NC ratios, along with cartoons illustrating the growth of the Au regions in the cores of the Au−InAs NPs. All data points correspond to the final states measured ca. 60 h after synthesis. The behavior of the In−O

regions, independently analyzed by EXAFS and XANES, are in excellent agreement with each other.

As shown by XAFS, STEM, and XRD, as the Au/InAs ratio increases, the Au core size increases and the extent of disorder in the InAs phase increases. Formation of such a crystalline metal core and disordered semiconductor shell is intriguing. Often, when two materials react and diffuse in nanocrystals, the nanoscale Kirkendall effect has been reported,[82] leading to the formation of voids and, ultimately, to hollow nanoparticles. The conditions for the Kirkendall effect are that the inward diffusing material diffuses slower than the outward diffusing material, but what happens when the material diffusing inward has a faster diffusion rate than the one diffusing outward? In this case, the inward diffusing material can form a crystalline core. The outward diffusing materials, on the other hand, due to the difference in the diffusion rate, will end up in the shell and may, in principle, also contain voids. However, these voids can merge with the outer surface or be manifested as a porous shell. These details should depend on the dimensions of the nanoparticle, the metal/NC ratio, and/or the difference in the diffusion rates.

The system presented herein is a case study for this reversed nanoscale Kirkendall effect. All of our observations can be explained in this framework. The Au core/InAs shell structure was formed as a result of this mechanism. Considering that Au diffuses inward faster than In and As diffuse outward, a crystalline Au core is formed without hollow regions. On the other hand, the InAs shell is porous and disordered (Figure 2c, inset).

◼ CONCLUSIONS

A study of the diffusion of Au atoms through the lattice of InAs NCs was carried out. XAFS measurements revealed that Au substitutes for In via a kick-out mechanism while moving toward the center of the NC to form a metallic Au core. Both XAFS and XRD measurements indicate that both the size of the metallic core and the extent of the disorder in the shell strongly depend on the initial Au/NC ratio. While XAFS analysis reveals the formation of In−O bonds, XRD measurements do not reflect the formation of an In_2O_3 phase. Control experiments performed by exposing the InAs NCs to either the ambient atmosphere or the same ligand composition revealed no formation of In−O bonds and no changes to the InAs structure, thus directly linking the observed changes and the diffusion of Au. The final Au−InAs core−shell is composed of a crystalline Au core and a disordered porous shell, as directly observed by STEM. Considering the larger diffusion coefficient for Au in
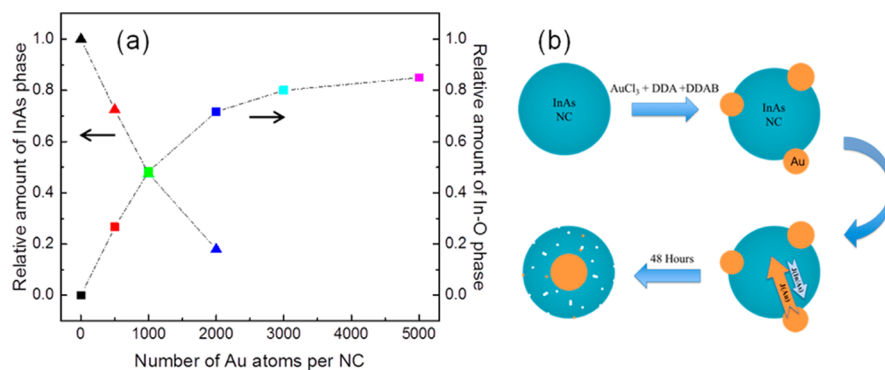

Figure 9. (a) Relative amounts of the InAs and In−O phases for Au−InAs NPs with different Au/NP ratios at 55 h after synthesis, obtained from EXAFS analysis for InAs and In−O; (b) schematic of the proposed diffusion process for Au−InAs NPs.

InAs[83] than for the self-diffusion of InAs,[84] Au can be considered a fast diffuser in InAs; therefore, the formation of the above structure can be rationalized through a reversed Kirkendall effect. This understanding can be used as a new way to synthesize unique nanoscale core−shell structures.

■ ASSOCIATED CONTENT

Ⓢ Supporting Information

The Supporting Information is available free of charge on the ACS Publications website at DOI: 10.1021/acs.chemmater.6b03779.

> Additional XAFS and XRD results; fitting results of the Au L$_3$-, Au L$_2$-, and In K-edge of InAs NPs (PDF)

■ AUTHOR INFORMATION

Corresponding Authors
*E-mail: uri.banin@mail.huji.ac.il (U.B.).
*E-mail: anatoly.frenkel@stonybrook.edu (A.I.F.).

Author Contributions
¶J.L. and Y.A. contributed equally to this work.

Notes
The authors declare no competing financial interest.

■ ACKNOWLEDGMENTS

■ REFERENCES

(1) Alivisatos, A. P. Perspectives on the Physical Chemistry of Semiconductor Nanocrystals. *J. Phys. Chem.* **1996**, *100*, 13226−13239.

(2) Brus, L. E. A Simple Model for the Ionization Potential, Electron Affinity, and Aqueous Redox Potentials of Small Semiconductor Crystallites. *J. Chem. Phys.* **1983**, *79*, 5566−5571.

(3) Peng, X.; Manna, L.; Yang, W.; Wickham, J.; Scher, E.; Kadavanich, A.; Alivisatos, A. P. Shape Control of CdSe Nanocrystals. *Nature* **2000**, *404*, 59−61.

(4) Lu, W.; Fang, J.; Ding, Y.; Wang, Z. L. Formation of PbSe Nanocrystals: A Growth toward Nanocubes. *J. Phys. Chem. B* **2005**, *109*, 19219−19222.

(5) Jin, R.; Cao, Y.; Mirkin, C. A.; Kelly, K. L.; Schatz, G. C.; Zheng, J. G. Photoinduced Conversion of Silver Nanospheres to Nanoprisms. *Science* **2001**, *294*, 1901−1903.

(6) Caswell, K. K.; Bender, C. M.; Murphy, C. J. Seedless, Surfactantless Wet Chemical Synthesis of Silver Nanowires. *Nano Lett.* **2003**, *3*, 667−669.

(7) Jen-La Plante, I.; Mokari, T. Harnessing Thermal Expansion Mismatch to Form Hollow Nanoparticles. *Small* **2013**, *9*, 56−60.

(8) Talapin, D. V.; Nelson, J. H.; Shevchenko, E. V.; Aloni, S.; Sadtler, B.; Alivisatos, A. P. Seeded Growth of Highly Luminescent CdsSe/CdS Nanoheterostructures with Rod and Tetrapod Morphologies. *Nano Lett.* **2007**, *7*, 2951−2959.

(9) Rivest, J. B.; Swisher, S. L.; Fong, L.-K.; Zheng, H.; Alivisatos, A. P. Assembled Monolayer Nanorod Heterojunctions. *ACS Nano* **2011**, *5*, 3811−3816.

(10) Sitt, A.; Salant, A.; Menagen, G.; Banin, U. Highly Emissive Nano Rod-in-Rod Heterostructures with Strong Linear Polarization. *Nano Lett.* **2011**, *11*, 2054−2060.

(11) Costi, R.; Saunders, A. E.; Banin, U. Colloidal Hybrid Nanostructures: A New Type of Functional Materials. *Angew. Chem., Int. Ed.* **2010**, *49*, 4878−4897.

(12) Banin, U.; Ben-Shahar, Y.; Vinokurov, K. Hybrid Semiconductor−Metal Nanoparticles: From Architecture to Function. *Chem. Mater.* **2014**, *26*, 97−110.

(13) Pescaglini, A.; Iacopino, D. Metal Nanoparticle-Semiconductor Nanowire Hybrid Nanostructures for Plasmon-Enhanced Optoelectronics and Sensing. *J. Mater. Chem. C* **2015**, *3*, 11785−11800.

(14) Liu, H.; Feng, Y.; Chen, D.; Li, C.; Cui, P.; Yang, J. Noble Metal-Based Composite Nanomaterials Fabricated Via Solution-Based Approaches. *J. Mater. Chem. A* **2015**, *3*, 3182−3223.

(15) Yuhas, B. D.; Habas, S. E.; Fakra, S. C.; Mokari, T. Probing Compositional Variation within Hybrid Nanostructures. *ACS Nano* **2009**, *3*, 3369−3376.

(16) Wood, A.; Giersig, M.; Mulvaney, P. Fermi Level Equilibration in Quantum Dot−Metal Nanojunctions. *J. Phys. Chem. B* **2001**, *105*, 8810−8815.

(17) Subramanian, V.; Wolf, E. E.; Kamat, P. V. Green Emission to Probe Photoinduced Charging Events in ZnO−Au Nanoparticles. Charge Distribution and Fermi-Level Equilibration. *J. Phys. Chem. B* **2003**, *107*, 7479−7485.

(18) Subramanian, V.; Wolf, E. E.; Kamat, P. V. Catalysis with TiO$_2$/Gold Nanocomposites. Effect of Metal Particle Size on the Fermi Level Equilibration. *J. Am. Chem. Soc.* **2004**, *126*, 4943−4950.

(19) Hirakawa, T.; Kamat, P. V. Charge Separation and Catalytic Activity of Ag@TiO$_2$ Core−Shell Composite Clusters under UV−Irradiation. *J. Am. Chem. Soc.* **2005**, *127*, 3928−3934.

(20) Mokari, T.; Rothenberg, E.; Popov, I.; Costi, R.; Banin, U. Selective Growth of Metal Tips onto Semiconductor Quantum Rods and Tetrapods. *Science* **2004**, *304*, 1787−1790.

(21) Mokari, T.; Sztrum, C. G.; Salant, A.; Rabani, E.; Banin, U. Formation of Asymmetric One-Sided Metal-Tipped Semiconductor Nanocrystal Dots and Rods. *Nat. Mater.* **2005**, *4*, 855−863.

(22) Saunders, A. E.; Popov, I.; Banin, U. Synthesis of Hybrid CdS−Au Colloidal Nanostructures. *J. Phys. Chem. B* **2006**, *110*, 25421−25429.

(23) Yang, J.; Elim, H. I.; Zhang, Q.; Lee, J. Y.; Ji, W. Rational Synthesis, Self-Assembly, and Optical Properties of PbS−Au Heterogeneous Nanostructures Via Preferential Deposition. *J. Am. Chem. Soc.* **2006**, *128*, 11921−11926.

(24) Menagen, G.; Mocatta, D.; Salant, A.; Popov, I.; Dorfs, D.; Banin, U. Selective Gold Growth on CdSe Seeded CdS Nanorods. *Chem. Mater.* **2008**, *20*, 6900−6902.

(25) Khalavka, Y.; Sönnichsen, C. Growth of Gold Tips onto Hyperbranched CdTe Nanostructures. *Adv. Mater.* **2008**, *20*, 588−591.

(26) Yang, J.; Ying, J. Y. Nanocomposites of Ag$_2$S and Noble Metals. *Angew. Chem., Int. Ed.* **2011**, *50*, 4637−4643.

(27) Li, P.; Wei, Z.; Wu, T.; Peng, Q.; Li, Y. Au−ZnO Hybrid Nanopyramids and Their Photocatalytic Properties. *J. Am. Chem. Soc.* **2011**, *133*, 5660−5663.

(28) Lee, J.-S.; Shevchenko, E. V.; Talapin, D. V. Au−PbS Core−Shell Nanocrystals: Plasmonic Absorption Enhancement and Electrical Doping Via Intra-Particle Charge Transfer. *J. Am. Chem. Soc.* **2008**, *130*, 9673−9675.

(29) Yang, J.; Ying, J. Y. Room-Temperature Synthesis of Nanocrystalline Ag$_2$S and Its Nanocomposites with Gold. *Chem. Commun.* **2009**, 3187−3189.

(30) Manzi, A.; Simon, T.; Sonnleitner, C.; Döblinger, M.; Wyrwich, R.; Stern, O.; Stolarczyk, J. K.; Feldmann, J. Light-Induced Cation Exchange for Copper Sulfide Based CO$_2$ Reduction. *J. Am. Chem. Soc.* **2015**, *137*, 14007−14010.

(31) Chen, W.-T.; Yang, T.-T.; Hsu, Y.-J. Au-CdS Core−Shell Nanocrystals with Controllable Shell Thickness and Photoinduced Charge Separation Property. *Chem. Mater.* **2008**, *20*, 7204−7206.

(32) Li, M.; Yu, X.-F.; Liang, S.; Peng, X.-N.; Yang, Z.-J.; Wang, Y.-L.; Wang, Q.-Q. Synthesis of Au−CdS Core−Shell Hetero-Nanorods with Efficient Exciton−Plasmon Interactions. *Adv. Funct. Mater.* **2011**, *21*, 1788−1794.

(33) Achermann, M. Exciton−Plasmon Interactions in Metal−Semiconductor Nanostructures. *J. Phys. Chem. Lett.* **2010**, *1*, 2837−2843.

(34) Costi, R.; Saunders, A. E.; Elmalem, E.; Salant, A.; Banin, U. Visible Light-Induced Charge Retention and Photocatalysis with Hybrid CdSe−Au Nanodumbbells. *Nano Lett.* **2008**, *8*, 637−641.

(35) Costi, R.; Cohen, G.; Salant, A.; Rabani, E.; Banin, U. Electrostatic Force Microscopy Study of Single Au−CdSe Hybrid Nanodumbbells: Evidence for Light-Induced Charge Separation. *Nano Lett.* **2009**, *9*, 2031−2039.

(36) Elmalem, E.; Saunders, A. E.; Costi, R.; Salant, A.; Banin, U. Growth of Photocatalytic CdSe−Pt Nanorods and Nanonets. *Adv. Mater.* **2008**, *20*, 4312−4317.

(37) Ben-Shahar, Y.; Scotognella, F.; Waiskopf, N.; Kriegel, I.; Dal Conte, S.; Cerullo, G.; Banin, U. Effect of Surface Coating on the Photocatalytic Function of Hybrid CdS−Au Nanorods. *Small* **2015**, *11*, 462−471.

(38) Ben-Shahar, Y.; Scotognella, F.; Kriegel, I.; Moretti, L.; Cerullo, G.; Rabani, E.; Banin, U. Optimal Metal Domain Size for Photocatalysis with Hybrid Semiconductor-Metal Nanorods. *Nat. Commun.* **2016**, *7*, 10413.

(39) Lavieville, R.; Zhang, Y.; Casu, A.; Genovese, A.; Manna, L.; Di Fabrizio, E.; Krahne, R. Charge Transport in Nanoscale "All-Inorganic" Networks of Semiconductor Nanorods Linked by Metal Domains. *ACS Nano* **2012**, *6*, 2940−2947.

(40) Hyun, J. K.; Lauhon, L. J. Spatially Resolved Plasmonically Enhanced Photocurrent from Au Nanoparticles on a Si Nanowire. *Nano Lett.* **2011**, *11*, 2731−2734.

(41) Pescaglini, A.; Martín, A.; Cammi, D.; Juska, G.; Ronning, C.; Pelucchi, E.; Iacopino, D. Hot-Electron Injection in Au Nanorod−ZnO Nanowire Hybrid Device for Near-Infrared Photodetection. *Nano Lett.* **2014**, *14*, 6202−6209.

(42) Yin, Y.; Rioux, R. M.; Erdonmez, C. K.; Hughes, S.; Somorjai, G. A.; Alivisatos, A. P. Formation of Hollow Nanocrystals through the Nanoscale Kirkendall Effect. *Science* **2004**, *304*, 711−714.

(43) Cabot, A.; Smith, R. K.; Yin, Y.; Zheng, H.; Reinhard, B. M.; Liu, H.; Alivisatos, A. P. Sulfidation of Cadmium at the Nanoscale. *ACS Nano* **2008**, *2*, 1452−1458.

(44) Shao, H.-F.; Qian, X.-F.; Zhu, Z.-K. The Synthesis of ZnS Hollow Nanospheres with Nanoporous Shell. *J. Solid State Chem.* **2005**, *178*, 3522−3528.

(45) Wang, Y.; Cai, L.; Xia, Y. Monodisperse Spherical Colloids of Pb and Their Use as Chemical Templates to Produce Hollow Particles. *Adv. Mater.* **2005**, *17*, 473−477.

(46) Liang, H.-P.; Guo, Y.-G.; Zhang, H.-M.; Hu, J.-S.; Wan, L.-J.; Bai, C.-L. Controllable AuPt Bimetallic Hollow Nanostructures. *Chem. Commun.* **2004**, 1496−1497.

(47) Zheng, J.; Song, X.; Zhang, Y.; Li, Y.; Li, X.; Pu, Y. Nanosized Aluminum Nitride Hollow Spheres Formed through a Self-Templating Solid−Gas Interface Reaction. *J. Solid State Chem.* **2007**, *180*, 276−283.

(48) Wang, C. M.; Baer, D. R.; Thomas, L. E.; Amonette, J. E.; Antony, J.; Qiang, Y.; Duscher, G. Void Formation During Early Stages of Passivation: Initial Oxidation of Iron Nanoparticles at Room Temperature. *J. Appl. Phys.* **2005**, *98*, 094308.

(49) Nakamura, R.; Lee, J. G.; Tokozakura, D.; Mori, H.; Nakajima, H. Formation of Hollow ZnO through Low-Temperature Oxidation of Zn Nanoparticles. *Mater. Lett.* **2007**, *61*, 1060−1063.

(50) Nakamura, R.; Tokozakura, D.; Nakajima, H.; Lee, J.-G.; Mori, H. Hollow Oxide Formation by Oxidation of Al and Cu Nanoparticles. *J. Appl. Phys.* **2007**, *101*, 074303.

(51) Kellogg, G. L. Field Ion Microscope Studies of Single-Atom Surface Diffusion and Cluster Nucleation on Metal Surfaces. *Surf. Sci. Rep.* **1994**, *21*, 1−88.

(52) Tsong, T. T. Quantitative Investigations of Atomic Processes on Metal Surfaces at Atomic Resolution. *Prog. Surf. Sci.* **1980**, *10*, 165−248.

(53) Zhang, Z.; Lagally, M. G. Atomistic Processes in the Early Stages of Thin-Film Growth. *Science* **1997**, *276*, 377−383.

(54) Tsong, T. T. Mechanisms of Surface Diffusion. *Prog. Surf. Sci.* **2001**, *67*, 235−248.

(55) Kellogg, G. L.; Feibelman, P. J. Surface Self-Diffusion on Pt(001) by an Atomic Exchange Mechanism. *Phys. Rev. Lett.* **1990**, *64*, 3143−3146.

(56) Chen, C.; Tsong, T. T. Displacement Distribution and Atomic Jump Direction in Diffusion of Ir Atoms on the Ir(001) Surface. *Phys. Rev. Lett.* **1990**, *64*, 3147−3150.

(57) Tsong, T. T.; Chen, C.-L. Atomic Replacement and Vacancy Formation and Annihilation on Iridium Surfaces. *Nature* **1992**, *355*, 328−331.

(58) Willoughby, A. F. W. Atomic Diffusion in Semiconductors. *Rep. Prog. Phys.* **1978**, *41*, 1665.

(59) Tuck, B. *Introduction to Diffusion in Semiconductors*; Peter Peregrinus: Stevenage, 1974.

(60) Dunlap, W. C. Diffusion of Impurities in Germanium. *Phys. Rev.* **1954**, *94*, 1531−1540.

(61) Weisberg, L. R.; Blanc, J. Diffusion with Interstitial-Substitutional Equilibrium. Zinc in GaAs. *Phys. Rev.* **1963**, *131*, 1548−1552.

(62) Myers, H. P. *Introductory Solid State Physics*; Taylor & Francis: London, 1981.

(63) Frank, F. C.; Turnbull, D. Mechanism of Diffusion of Copper in Germanium. *Phys. Rev.* **1956**, *104*, 617−618.

(64) Aleksandrov, O. V.; Krivoruchko, A. A. Out-Diffusion of Impurity Via the Kick-out Mechanism During Gettering. *Semiconductors* **2007**, *41*, 1048−1055.

(65) Gosele, U. M. Fast Diffusion in Semiconductors. *Annu. Rev. Mater. Sci.* **1988**, *18*, 257−282.

(66) Mokari, T.; Aharoni, A.; Popov, I.; Banin, U. Diffusion of Gold into Inas Nanocrystals. *Angew. Chem., Int. Ed.* **2006**, *45*, 8001−8005.

(67) Franchini, I. R.; Bertoni, G.; Falqui, A.; Giannini, C.; Wang, L. W.; Manna, L. Colloidal PbTe-Au Nanocrystal Heterostructures. *J. Mater. Chem.* **2010**, *20*, 1357−1366.

(68) Amit, Y.; Eshet, H.; Faust, A.; Patllola, A.; Rabani, E.; Banin, U.; Frenkel, A. I. Unraveling the Impurity Location and Binding in Heavily Doped Semiconductor Nanocrystals: The Case of Cu in InAs Nanocrystals. *J. Phys. Chem. C* **2013**, *117*, 13688−13696.

(69) Amit, Y.; Li, Y.; Frenkel, A. I.; Banin, U. From Impurity Doping to Metallic Growth in Diffusion Doping: Properties and Structure of Silver-Doped InAs Nanocrystals. *ACS Nano* **2015**, *9*, 10790−10800.

(70) Mocatta, D.; Cohen, G.; Schattner, J.; Millo, O.; Rabani, E.; Banin, U. Heavily Doped Semiconductor Nanocrystal Quantum Dots. *Science* **2011**, *332*, 77−81.

(71) Menard, L. D.; Wang, Q.; Kang, J. H.; Sealey, A. J.; Girolami, G. S.; Teng, X.; Frenkel, A. I.; Nuzzo, R. G. Structural Characterization of Bimetallic Nanomaterials with Overlapping X-ray Absorption Edges. *Phys. Rev. B: Condens. Matter Mater. Phys.* **2009**, *80*, 064111.

(72) Cao; Banin, U. Growth and Properties of Semiconductor Core/Shell Nanocrystals with InAs Cores. *J. Am. Chem. Soc.* **2000**, *122*, 9692−9702.

(73) Ravel, B.; Newville, M. Athena, Artemis, Hephaestus: Data Analysis for X-ray Absorption Spectroscopy Using IFEFFIT. *J. Synchrotron Radiat.* **2005**, *12*, 537−541.

(74) Newville, M. Ifeffit: Interactive XAFS Analysis and FEFF Fitting. *J. Synchrotron Radiat.* **2001**, *8*, 322−324.

(75) Frenkel, A. I.; Cason, M. W.; Elsen, A.; Jung, U.; Small, M. W.; Nuzzo, R. G.; Vila, F. D.; Rehr, J. J.; Stach, E. A.; Yang, J. C. Critical Review: Effects of Complex Interactions on Structure and Dynamics of Supported Metal Catalysts. *J. Vac. Sci. Technol., A* **2014**, *32*, 020801.

(76) Frenkel, A. I.; Hills, C. W.; Nuzzo, R. G. A View from the Inside: Complexity in the Atomic Scale Ordering of Supported Metal Nanoparticles. *J. Phys. Chem. B* **2001**, *105*, 12689−12703.

(77) Frenkel, A. I.; Nemzer, S.; Pister, I.; Soussan, L.; Harris, T.; Sun, Y.; Rafailovich, M. H. Size-Controlled Synthesis and Characterization

of Thiol-Stabilized Gold Nanoparticles. *J. Chem. Phys.* **2005**, *123*, 184701.

(78) Sanchez, S. I.; Menard, L. D.; Bram, A.; Kang, J. H.; Small, M. W.; Nuzzo, R. G.; Frenkel, A. I. The Emergence of Nonbulk Properties in Supported Metal Clusters: Negative Thermal Expansion and Atomic Disorder in Pt Nanoclusters Supported on γ-Al$_2$O$_3$. *J. Am. Chem. Soc.* **2009**, *131*, 7040−7054.

(79) Sun, Y.; Frenkel, A. I.; Isseroff, R.; Shonbrun, C.; Forman, M.; Shin, K.; Koga, T.; White, H.; Zhang, L.; Zhu, Y.; Rafailovich, M. H.; Sokolov, J. C. Characterization of Palladium Nanoparticles by Using X-ray Reflectivity, EXAFS, and Electron Microscopy. *Langmuir* **2006**, *22*, 807−816.

(80) Frenkel, A. Solving the 3D Structure of Metal Nanoparticles. *Z. Kristallogr. - Cryst. Mater.* **2007**, *222*, 605−611.

(81) Glasner, D.; Frenkel, A. I. Geometrical Characteristics of Regular Polyhedra: Application to EXAFS Studies of Nanoclusters. *AIP Conf. Proc.* **2006**, *882*, 746−748.

(82) Wang, W.; Dahl, M.; Yin, Y. Hollow Nanocrystals through the Nanoscale Kirkendall Effect. *Chem. Mater.* **2013**, *25*, 1179−1189.

(83) Indium Arsenide (InAs), Vibrational Modes of Impurities. In *Impurities and Defects in Group IV Elements, IV-IV and III-V Compounds. Part B: Group IV-IV and III-V Compounds*; Madelung, O., Rössler, U., Schulz, M., Eds.; Springer Berlin Heidelberg: Berlin, 2003; pp 1−2.

(84) Kato, H.; Yokozawa, M.; Kohara, R.; Okabayashi, Y.; Takayanagi, S. Self-Diffusion in InAs Crystals. *Solid-State Electron.* **1969**, *12*, 137−139.